Stability profile of transition metal oxides in the oxygen evolution reaction in alkaline medium

*Aliki Moysiadou and Xile Hu**

Laboratory of Inorganic Synthesis and Catalysis, Institute of Chemical Sciences and Engineering, École Polytechnique Fédérale de Lausanne (EPFL), ISIC-LSCI, 1015 Lausanne, Switzerland

* E-mail: xile.hu@epfl.ch

KEYWORDS: Electrocatalysis, oxides, oxygen evolution reaction, stability.

ABSTRACT: The electrochemical water splitting reaction can convert renewable electricity into clean hydrogen fuel. The efficiency of water splitting is limited to a large extend by the sluggish oxygen evolution reaction (OER). Numerous transition metal oxides have been developed as electrocatalysts for OER in alkaline medium. However, in-depth studies of the stability of these catalysts have rarely been performed. Here we report a systematic investigation of the stability profile of five archetypical OER catalysts including CoO_x, $CoFeO_x$, $CoFeNiO_x$, NiO_x, and $NiFeO_x$. We combine measurements of electrochemical activity, electrochemical quartz crystal microbalance (eQCM), inductively coupled plasma optical emission spectrometry (ICP-OES), and electrochemical impedance spectroscopy (EIS). We find that eQCM gives incorrect information of the mass change during OER due to non-ideal response, and confirm that activity is not a valid descriptor of stability. Of the five oxides, CoO_x and $CoFeO_x$ lose some mass during an initial period of OER while $CoFeNiO_x$, NiO_x, and $NiFeO_x$ maintain their mass. However, all five catalysts undergo noticeable compositional changes due to a dynamic exchange of metal ions with the

electrolyte solutions. Partial dissolution of CoO_x and incorporation of Fe ions are the main processes of this exchange. The dynamic exchange reaches equilibrium after 6 h, and the catalysts are stable afterwards.

INTRODUCTION

The electrochemical water splitting reaction provides a means to convert renewable electricity from solar and wind into hydrogen, a clean energy carrier.[1–3] The water splitting reaction consists of two electrochemical half-reactions, namely the hydrogen evolution reaction (HER; $2H^+ + 2e^- \rightarrow H_2$) and the oxygen evolution reaction (OER; $2H_2O \rightarrow O_2 + 4H^+ + 4e^-$). Both HER and OER require efficient electrocatalysts to operate at practical rates, but OER is kinetically more complex and demands a larger overpotential than HER.[4–6] There is a renaissance of studies of transition metal oxides as OER catalysts in alkaline medium.[4,5,7–12] Much focus has been put on the activity of catalysts. While stability is an equally important quality metric to activity, systematic studies of stability of OER catalysts only start to emerge.[13–18]

Activity monitoring during a few hours of electrolysis or potentiodynamic measurements are commonly used methods to probe the stability of OER catalysts. For example, McCrory et al.[19] used a protocol based on electrolysis at 10 mA cm^{-2} during 2 hours to assess the short-term stability of OER catalysts in alkaline solutions. This method is easy to use and can quickly reveal very instable catalysts. However, it cannot provide a rigorous measure of stability because a catalyst can maintain its macroscopic activity while undergoing partial deactivation or decomposition as long as it has sufficient active sites. The change of the mass of a catalyst during operation, on the other hand, provides direct information of the stability of the catalyst. The change of mass can be detected by inductively coupled plasma (ICP) spectrometry. Experimental setups comprising an electrochemical flow cell and an ICP-Mass Spectrometer (MS) or ICP-Optical Emission Spectrometry (OES) have been developed to probe in-situ the mass change of OER catalysts.[20,21] Notwithstanding their utility, these setups are not easily accessible to most research groups in the field. Electrochemical quartz crystal microbalance (eQCM) is an alternative, commercially available tool to monitor the mass change of catalysts during operation. eQCM is highly sensitive and can detect small mass changes on the order of 1 ng.[22] Using eQCM, Boettcher and co-workers[23,24] investigated the mass changes of several transition metal oxides during short-term electrolysis (e.g., 4 h) in alkaline solutions at modest overpotentials (e.g., 350 mV). The drawback of eQCM, however, is that the observed mass change might be caused by factors other than dissolution or re-deposition of catalysts, such as absorption and desorption of ions and solvents.[25,26] Indeed the limitation of eQCM was noted in a previous study of the stability of RuO_x and MnO_x.[27]

Here we report a study of the stability profile of Fe, Co, and Ni-containing unary, binary, and tertiary oxides in OER in alkaline medium. These oxides are archetypical OER catalysts. We combined eQCM, ICP–OES, and electrochemical impedance spectroscopy (EIS) in this study, which overcame the limitation of using eQCM alone. The results reveal a complex, catalyst-depending stability profile of these oxides.

EXPERIMENTAL SECTION

Preparation of catalysts. Thin films of CoO_x, NiO_x, $CoFeO_x$, $CoFeNiO_x$ were prepared by linear sweep voltammetry at oxidative potentials at a scan rate of 10 mV s^{-1}, following our previously reported method.[28] The potential window for CoO_x and NiO_x was set to 1.7–2.0 V vs. the reversible hydrogen electrode (RHE). The oxidative deposition of Fe-containing catalysts was complicated by occasionally a spontaneous precipitation of an insoluble residue, presumably a trinuclear acetate cluster,[29,30] in the deposition bath and significant bubble (oxygen) formation during electrodeposition. These problems were remediated by applying a potential window of 1.70–1.85 V vs. RHE for the deposition. Thin films of $NiFeO_x$ were prepared by reductive deposition at a constant a current density of -0.1 mA cm^{-2}.[31] The initial loadings of the catalysts were controlled by changing the number of linear sweeps for oxidative depositions and the duration of deposition for the reductive deposition.

All electrochemical experiments were performed in a single-compartment, three-electrode electrochemical Teflon cell at room temperature, using a Methrom Autolab potentiostat/galvanostat. Milli-pore water (18.3 MΩ cm) and analytical grade reagents were employed. CoO_x and NiO_x were prepared from aqueous solutions of 0.016 M cobalt(II) chloride ($CoCl_2$, anhydrous, >98%, Fluka) and 0.016 M nickel(II) acetate (NiOAc, tetrahydrate, 98%, Sigma-Aldrich), respectively, which also contained 0.1 M sodium acetate (NaOAc, anhydrous, ≥ 99%, Sigma-Aldrich). $CoFeO_x$, and $CoFeNiO_x$ were deposited from similar baths which contained additionally 0.005 M iron(III) sulfate ($Fe_2(SO_4)_3$, hydrate, 97%, Sigma-Aldrich). $NiFeO_x$ was reductively deposited from aqueous solutions of 0.008 M iron (II) chloride ($FeCl_2$, tetrahydrate, ≥ 99%, Sigma-Aldrich) and 0.092 M nickel (II) nitrate ($Ni(NO_3)_2$, hexahydrate, Sigma-Aldrich) following a reported deposition procedure.[14,32,33] During the cathodic deposition, the nitrate anions in the catholyte are reduced to nitrite ions leading to an increase of the local pH and the precipitation of the metal hydroxides. The catalysts were deposited on 10 MHz Au-coated quartz crystal electrodes (Gamry Instruments), which have an electrochemical surface area of 0.205 cm^2. On both faces of the quartz crystals there is a double layer of 10 nm Cr and 100 nm Au. The electrodes were cleaned by 1 M H_2SO_4 followed by a thorough washing with water. Prior to deposition, the surfaces of the electrodes were cycled in 1 M KOH from 0.00 to 1.65 V vs. RHE to confirm the absence of redox features related to residual impurities on the electrode surface.[34] We avoided cycling of the bare electrodes to potentials higher than 1.65 V vs. RHE to prevent oxidation of the Au substrate. For deposition, the counter electrode was a titanium wire and the reference electrode was a custom-made double-junction Ag/AgCl electrode in a saturated KCl solution (+ 0.197 V vs NHE at 25°C). The Teflon cell was immersed in 1 M H_2SO_4 solution when not used to prevent cross contamination between individual experiments.

Electrochemical tests. For electrochemical measurements, a three-electrode setup comprised an Au-coated quartz crystal as working electrode, a Pt-wire counter electrode, and a Hg/HgO/ 1M KOH reference electrode was used in a Teflon cell. Clean Pt surfaces were obtained by dipping the wire in aqua regia for a few seconds, rinsing it with copious amounts of water and annealing it with gas–O_2 flame. A polymenthyl pentane (PMP) tube encased the Hg/HgO reference electrode and a ceramic junction (ALS Co., Ltd) separated it from the alkaline reaction medium. The potential of the reference electrode was calibrated with respect to the reversible hydrogen electrode (RHE) by measuring the equilibrium potential for HER by a Pt wire working electrode in a 1M H_2-saturated KOH solution. The experiments were performed in both 1M unpurified KOH and 1M Fe-free KOH. The purification of the KOH (1 N standard solution, Merck KGaA, diluted with 18.2 MΩ cm H_2O) was performed following a procedure already reported in the literature.[31,34] For Co-based materials, the electrolyte was purified using $Co(NO_3)_2 \bullet 6H_2O$, while for Ni-based materials the electrolyte was purified using $Ni(NO_3)_2 \bullet 6H_2O$. An anion exchange membrane (AGFA's ZIRFON PERL; comprised of an open mesh polypropylene sulphide fabric symmetrically coated with a mixture of polymer and zirconium oxide,) was used to separate the working and counter electrodes. The activity of the electrocatalysts was measured by linear sweep voltammetry at a scan rate of 5mV s^{-1}.

eQCM was used to measure the mass of the catalyst films. The response of the Au-coated quartz crystals was calibrated by the deposition of Cu from a solution of $CuSO_4$. For in-situ monitoring of the evolution of mass during OER, the monitoring started after the frequency of the resonator was stable at the open circuit potential. The monitoring was done under potentiostatic and galvanostatic conditions for up to 14 h. The specific conditions were (i) at a constant current density of 5 mA cm^{-2}, and (ii) at a constant potential of 1.58 V vs. RHE. The electrolyte resistance was determined by electrochemical impedance spectroscopy (EIS) before and after electrolysis from the high frequency response. The uncompensated resistance was between 6 and 9 Ω in 1 M KOH depending on the configuration of the cell.

The impedance of the electrocatalysts was recorded in a frequency range from 10 kHz to 0.1 Hz. The amplitude of the applied alternating potential was 10 mV. The EIS response was measured at anodic potentials spanning from 1.47 to 1.58 V vs. RHE. Before the EIS measurement, the electrode was set to stabilize for 30 s at each respective potential. We analyzed and fitted the impedance data using Zview software. Based on the values of the double layer capacitance, C_{dl}, we calculated the ECSA at different potentials for each catalyst, assuming a specific capacitance of 40 µF cm^{-2}.[35] A value of 40 µF cm^{-2} in 1M NaOH for this type of materials has been used in the literature, although variations might be expected.[19,36,37]

Characterization methods. ICP-OES analyses were performed on as-deposited and post-catalytic samples by a Nexlon 350 (Perkin Elmer) machine. The samples were digested in 65% HNO_3 (Merck) and diluted in water to reach a final concentration of 2% w/w HNO_3. For each catalyst, the as-deposited samples at four different loadings were analyzed. The measurements were repeated three times, giving 12 samples for each catalyst. For post-catalytic analysis, samples of each catalyst at three different loadings were measured. The measurements were repeated three times, giving 9 samples per catalyst. Direct quantification of dissolved metals in the alkaline electrolyte was hindered by the high concentration of potassium (1M KOH).

Scanning Electron Microscopy (SEM). Surface characterization was performed with a Gemini field emission scanning electron microscope. A 1–3 kV accelerating voltage was chosen for the analysis. Secondary electrons were collected with an in-lens detector and the surfaces were imaged directly with no further treatment. Both as-prepared and after electrolysis samples were analysed.

X-ray Photoelectron Spectroscopy (XPS). X-ray photoelectron spectroscopy analyses were carried out using a PHI VersaProbe II scanning XPS microprobe (Physical Instruments AG, Germany). Monochromatic X-rays were generated by an Al Kα source of 24.8 W with a beam size of 100 µm. The spherical capacitor analyser was set at 45° take-off angle with respect to the sample surface. The pass energy was 46.95 eV yielding a full width at half maximum of 0.91 eV for the Ag 3d 5/2 peak. The adventitious carbon 1s peak was calibrated at 284.8 eV and used as an internal standard. XPS data analysis was performed using the PHI MultiPak software.

X-ray diffraction

The structure of the films was analyzed by X-ray diffraction (XRD) with a Bruker diffractometer (instrument type D8 Advance) using a Cu Kα non-monochromated X-ray source at 40kV and 40mA. The detector was scanned in the 2θ range from 10^{o} to 90^{o}. For the XRD analysis, the films were electrodeposited on gold substrates.

RESULTS

Loading and characterization of as-prepared thin-film catalysts. All the catalysts were prepared by electrodeposition, which made it possible to determine their loadings by eQCM. Once prepared, the catalysts could be dissolved and their amounts could be measured by ICP-OES. Figure 1 shows the results from eQCM and ICP-OES for all five catalysts. For each catalyst, the loadings determined by eQCM were lineally correlated to the loadings determined by ICP-OES. eQCM overestimated the loadings by roughly 100% (for CoO_x, $CoFeO_x$, and

$CoFeNiO_x$) or 25% (for NiO_x, and $NiFeO_x$). eQCM is based on the Sauerbrey equation ($\Delta m = -C_f \Delta f$), which correlates the change of the resonant frequency of a piezoelectric material with the change of mass on its surface.[22,25] However, surface roughness, change of viscoelastic properties, and bubble formation can lead to a significant deviation from the Sauerbrey response.[25,38,39] For example, surface adsorbed species as well as intercalated ions and water molecules could result in an adventitious mass component.[40] The results in Figure 1 indicate a non-ideal behaviour of the eQCM response for these metal oxides due to some of the above-mentioned factors. For CoO_x, $CoFeO_x$, and $CoFeNiO_x$, bubble formation due to OER was observed during electrodeposition, while for NiO_x and $NiFeO_x$, no bubble formation was observed. The larger overestimation by eQCM for the loadings of CoO_x, $CoFeO_x$, and $CoFeNiO_x$, therefore, seems to originate from the interference of oxygen bubbles. On the other hand, the linear correlations of the results from eQCM and ICP-OES suggests that the former can be used qualitatively to measure the loadings of the catalysts.

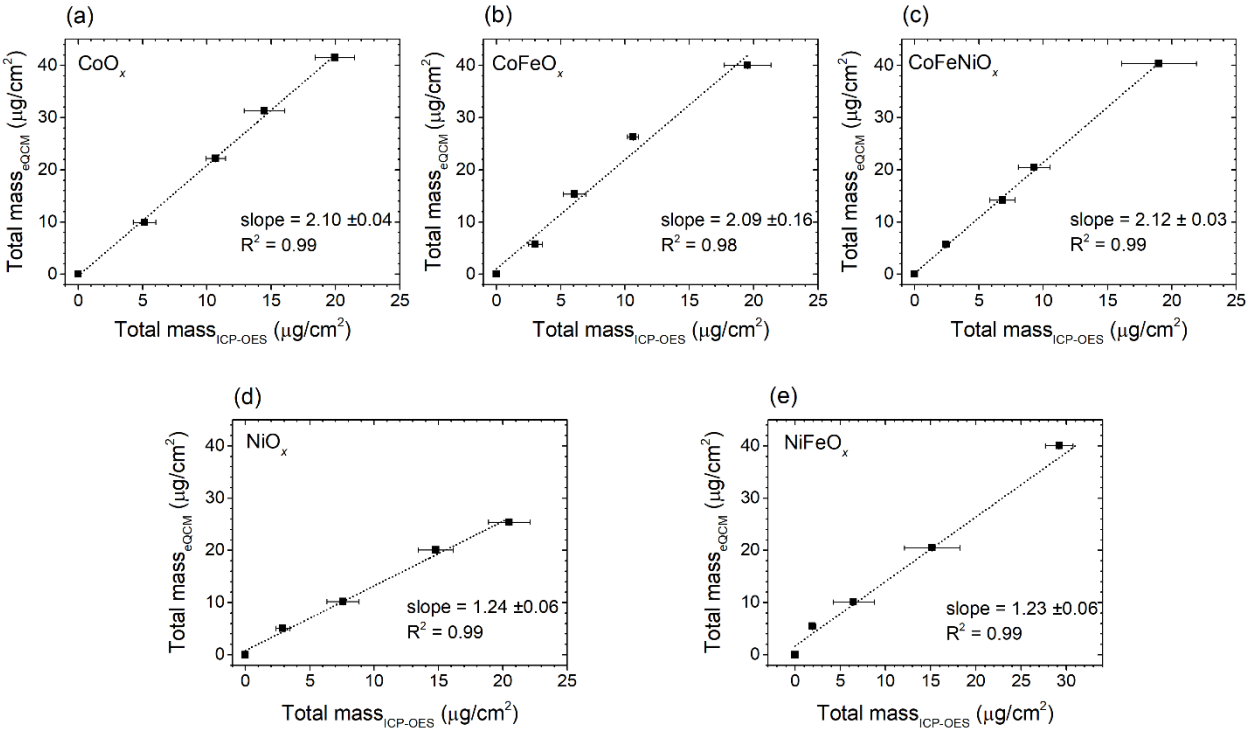

Figure 1. Correlations of the loadings of catalysts determined by eQCM and ICP-OES for five metal oxide OER catalysts. The error bars represent the standard deviation of three experimental data.

The chemical composition and oxidation state of the catalytic films were probed by XPS. Figures S2–S7 show the XPS spectra of as-prepared and after-electrolysis films of CoO_x, $CoFeO_x$, $CoFeNiO_x$, NiO_x and $NiFeO_x$. For

all Co-based materials, the high-resolution Co 2p spectrum shows spin-orbit splitting into two main peaks assigned to Co $2p_{1/2}$ and Co $2p_{3/2}$. The binding energy of the main Co $2p_{3/2}$ is at 780.4 eV corresponding to $Co(OH)_2$.[41–43] Further, we observe a broad satellite peak at 785.6 eV associated to the high-spin $Co(OH)_2$.[28] The Fe 2p high-resolution spectra is complicated due to spectral overlaps, which makes it difficult to assign peaks to specific iron oxides.[42,44] However, the oxidation state of iron can be identified as +3. These results are in accordance with previous reports.[28,45] The O 1s XPS signals are fitted with three separate peaks at 529.6 eV, 531.4 eV and 533 eV. The main peak at 531.4 eV is assigned to oxygen atoms of surface hydroxyl groups (OH^-), while the small one at 529.6 eV corresponds to lattice oxygen (O^{2-}). The third small peak around 533 eV observed is associated with adsorbed water molecules.[46,47] The Ni 2p spectrum shows a main $2p_{3/2}$ peak around 855.73 eV. Peaks of NiOOH and $Ni(OH)_2$ were reported to have binding energies of 855.75 and 855.80 eV, respectively.[42,46,48] However, the multiplet splitting of Ni $2p_{3/2}$ renders the assignment of the peaks to a sole oxidation state difficult. Overall, no obvious changes were observed for each catalyst before and after electrolysis.

The morphology of the catalyst films was investigated by Scanning Electron Microscopy (Figures S7-S11). The Co-based catalysts (CoO_x, $CoFeO_x$, and $CoFeNiO_x$) are composed of compact films with homogeneously distributed nodules. The NiO_x and $NiFeO_x$ catalysts are composed of a network of nanosheets. Again electrolysis did not result in a significant change of morphology. X-ray powder diffraction measurements (Figure S12) showed that all catalyst samples, both as-deposited and after-electrolysis, were X-ray.

Electrochemical activity of the as-prepared thin-film catalysts. The initial activity of these catalysts was measured and compared (Figure 2 and Table S1, SI). Analysis of linear sweep voltammetry (LSV) curves (Figure 2a) reveals different Tafel slopes for the catalysts (Figure 2b): 54 mV/dec for NiO_x, 45 mV/Dec for CoO_x, and about 40 mv/dec for $CoFeO_x$, $CoFeNiO_x$, and $NiFeO_x$. We used two parameters to compare the activity: specific activity, J_s, (Figure 2c) and turnover frequencies , TOF^{tm}, (Figure 2d).[5] The former was obtained by dividing the current (Figure 2a) by the electrochemical surface area (ECSA) determined by EIS. The latter was obtained by considering the total metal loadings of the catalysts determined by ICP-OES. A same order of activity was found: $NiO_x < CoO_x < CoFeO_x \approx CoFeNiO_x < NiFeO_x$. The results are consistent with previous reports.[24,28]

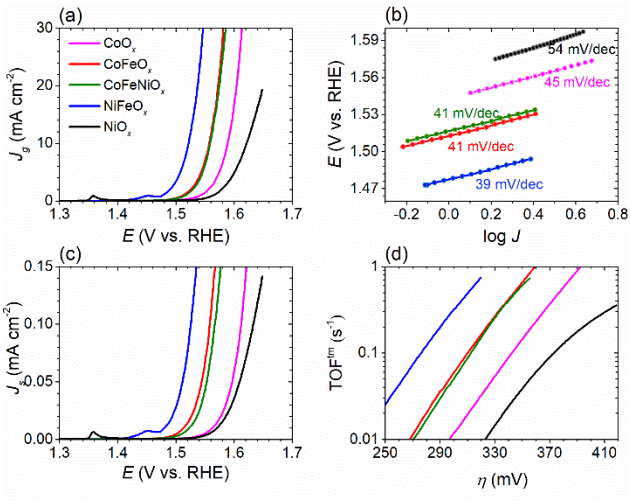

Figure 2. (a) LSV curves of catalysts measured in 1M KOH. Scan rate: 5 mV/s; the loadings of the catalysts were 20–25 μg cm^{-2} based on eQCM; (b) Tafel analysis of the LSV curves; (c) specific activity of the catalysts; (d) turnover frequencies of the catalysts.

Evolution of activity and catalyst mass during galvanostatic electrolysis. The as-prepared catalyst films were subjected to galvanostatic electrolysis at 5 mA/cm^2 for 6 hours. The activity of these films, manifested by potential, remained largely constant for $NiFeO_x$ (Figure 3e and Table S1, SI). The potentials, however, dropped by about 30 mV for CoO_x, NiO_x, $CoFeO_x$, and $CoFeNiO_x$, indicating improved activity (Figure 3a–d and Table S1, SI). The increase of activity for CoO_x and NiO_x is presumably due to the incorporation of residual Fe ion in commercial KOH electrolyte.[31] The increase of activity for $CoFeO_x$ and $CoFeNiO_x$ is probably due to an activation process, which seemed to complete after 2 hours.

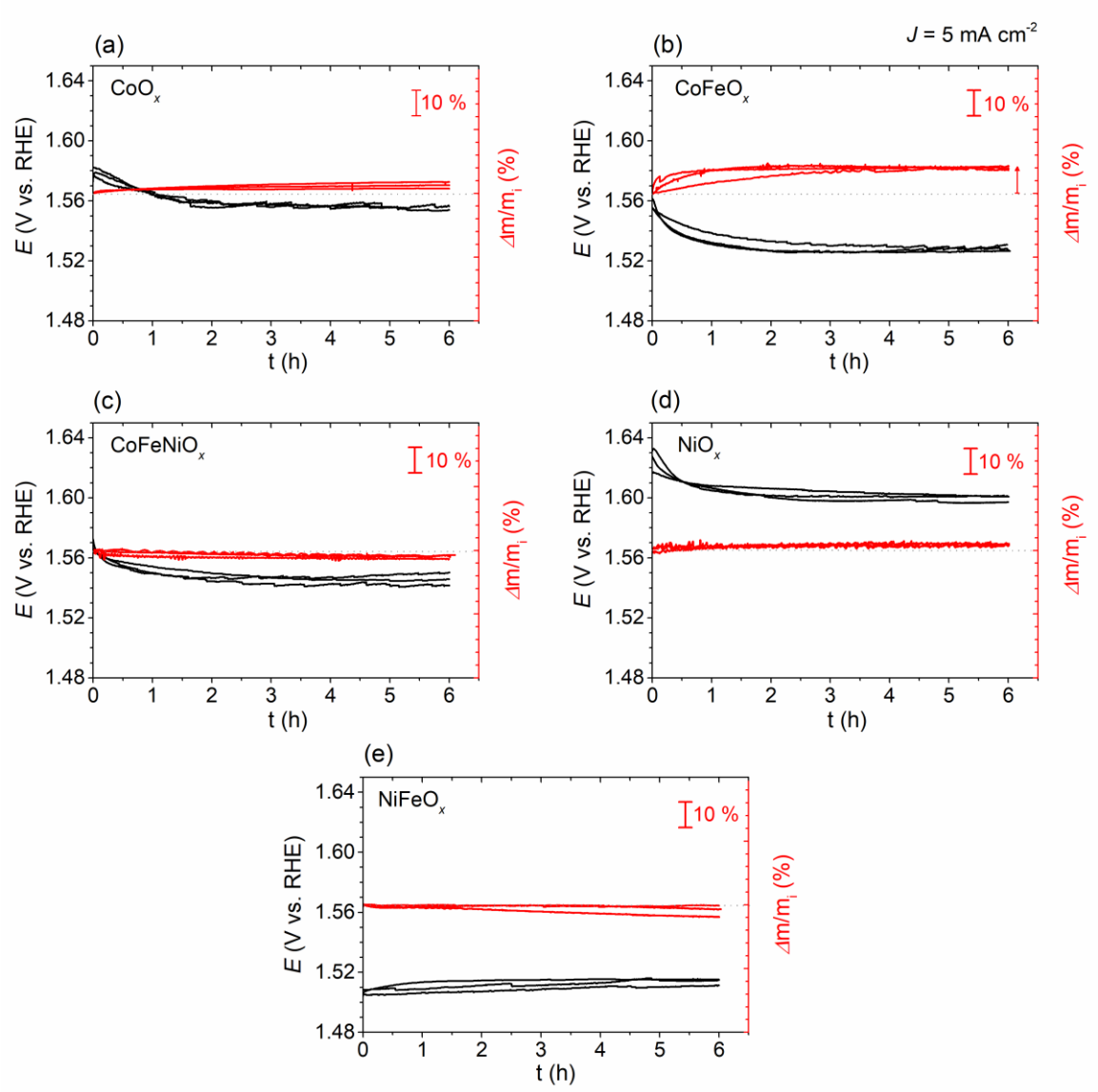

Figure 3. (a)-(e) Evolution of potential and mass of the five catalysts during electrolysis at a constant current density of 5 mA/cm^2 in 1 M KOH. The evolution of mass was determined by eQCM. Three samples were measured for each catalyst.

The evolution of catalyst mass was first monitored *in-situ* and *operando* by eQCM. Very little change in the mass of CoO_x, NiO_x, $NiFeO_x$, and $CoFeNiO_x$ was detected (Figure 3a, 3c–e). For $CoFeO_x$, an about 10% increase in mass was observed by eQCM (Figure 3b). A similar result was reported by Boettcher and co-workers[34], which showed a 1–7% mass increase for $Co_{1-x}Fe_x(OOH)$ (for $x < 0.5$) after 2 h of potentiostatic electrolysis detected by eQCM.

As the measurements of as-prepared films indicated that eQCM could give different results than ICP-OES (see above), the mass of the catalyst films after electrolysis were analysed by ICP-OES. The mass decreased by

about 20-30% for CoO_x and $CoFeO_x$ (Figure 4a, 4b). On the other hand, insignificant mass change was found for $CoFeNiO_x$, NiO_x, and $NiFeO_x$ (Figure 4c–4e). Overall, the results from eQCM and ICP-OES are in large disagreement. ICP-OES also permitted the detection of composition changes during catalysis. For both NiO_x and CoO_x, incorporation of Fe ions in the catalyst films was observed (Figure 4a, 4d), albeit in a small amount. The Fe incorporation, however, did not significantly alter the mass of NiO_x. For $CoFeO_x$ and $NiFeO_x$, an enrichment in Fe was found (Figure 4b, 4e).

The above experiments were conducted in commercial KOH solutions, which contained a trace amount of Fe ions.[14,31,49] We preferred to use these electrolyte solutions as they are more realistic than purified electrolytes where the Fe ions are depleted. The presence of Fe ions might influence the stability profile. Thus, we also analyzed the stability profile of the five catalysts in Fe-free electrolytes during galvanostatic electrolysis. The activity profiles are shown in Figure S13. The Co-based catalysts have stable activity over time. The activity of both NiO_x and $NiFeO_x$, on the other hand, decreased over time. Compared to the activity profiles measured in commercial, Fe-containing electrolytes, these results point to a strong impact of Fe ions in the OER activity of metal oxides. Previous reports [31,34,49–51] have already shown that Fe incorporation increases the activity of NiO_x and CoO_x films. [49] Our results further indicate that Fe impurities in the electrolytes can either stabilize the activity (e.g., $NiFeO_x$) or help to further activate Fe-containing metal oxides (e.g., $CoFeO_x$ and $CoFeO_x$).

ICP-OES measurements (Figure S14) were conducted to monitor the mass change after electrolysis in Fe-free electrolytes. As expected, no Fe incorporation was observed. Instead, mass increase due to deposition of CoO_x and NiO_x occurred. This deposition originated from the introduction of Ni or Co ions in the preparation of Fe-free electrolytes. Burke et al.[24] observed a similar increase in the mass of Co oxyhydroxide during OER in Fe-free, Co-containing electrolyte and attributed it to anodic cobalt oxide deposition. In our case, the deposition was more noticeable for mixed metal oxides ($CoFeO_x$, $CoFeNiO_x$, and $NiFeO_x$). Thus, Fe-free electrolytes, as they are prepared in today's methods, are not appropriate media for studying the stability profiles of metal oxides during OER. Accordingly, we continued our investigation using commercial KOH electrolytes, even though it contained a trace amount of Fe impurities.

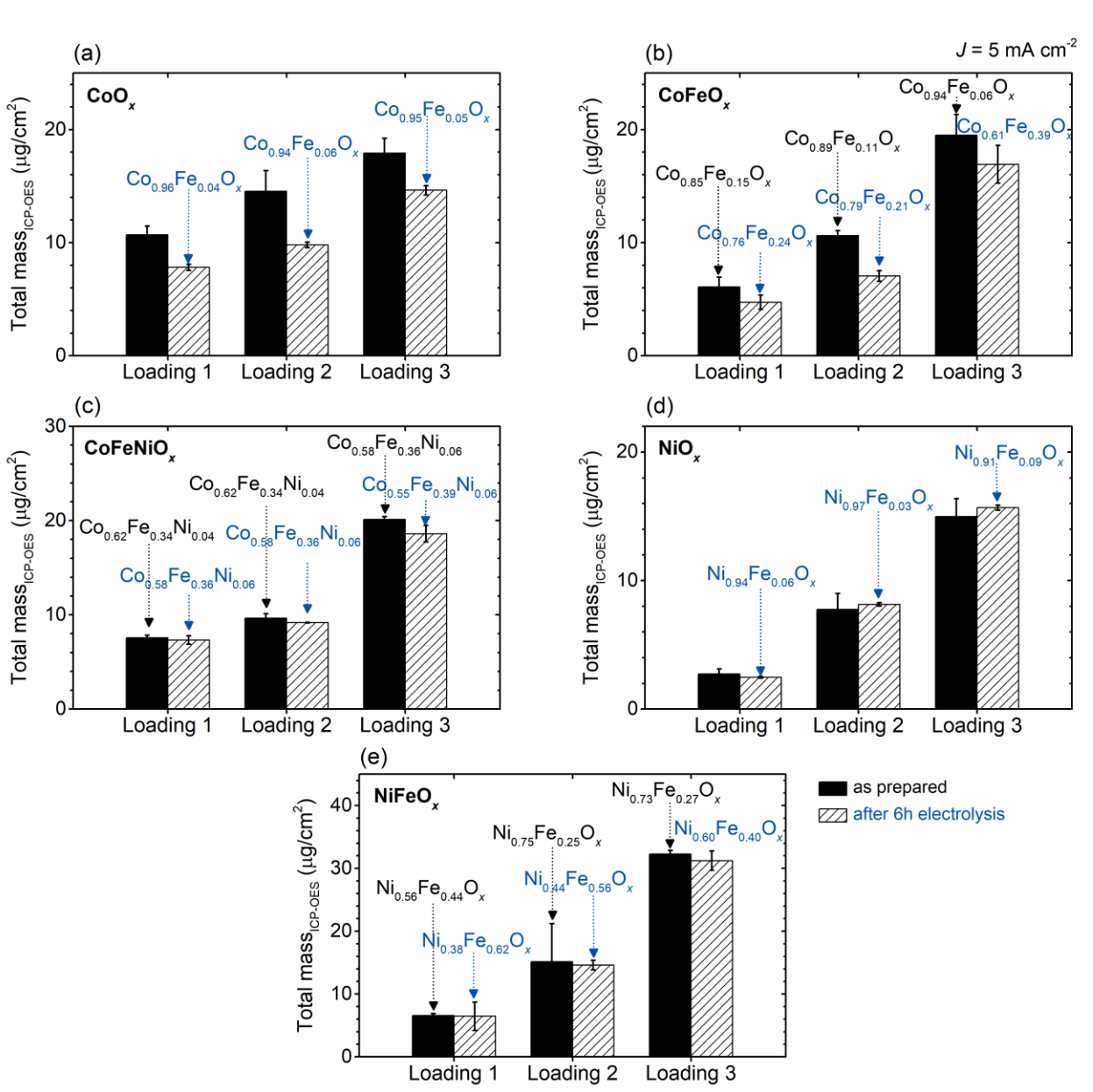

Figure 4. (a)-(f) Comparison of the mass of the catalysts before and after electrolysis at a constant current density of 5 mA/cm^2 for 6 h in 1 M KOH. The composition of the catalysts before and after catalysis is indicated.

Evolution of activity and catalyst mass during potentiostatic electrolysis. The as-prepared catalyst films were also subjected to potentiostatic electrolysis at E = 1.58 V vs RHE (i.e., an overpotential of 350 mV for OER) for 6 hours. The catalytic activity, as expressed by current densities, was stable for CoO_x, $CoFeO_x$, and $CoFeNiO_x$. The activity of NiO_x gradually increased, consistent with previous finding that incorporation of residual Fe ions in the electrolyte lead to a more active $NiFeO_x$ catalyst.[31] The significant variation in activity observed among different

samples of NiO_x was probably due to the irregularity of the Fe incorporation. The activity of $NiFeO_x$ was the highest. It decreased in the first hour to reach a relative stable value.

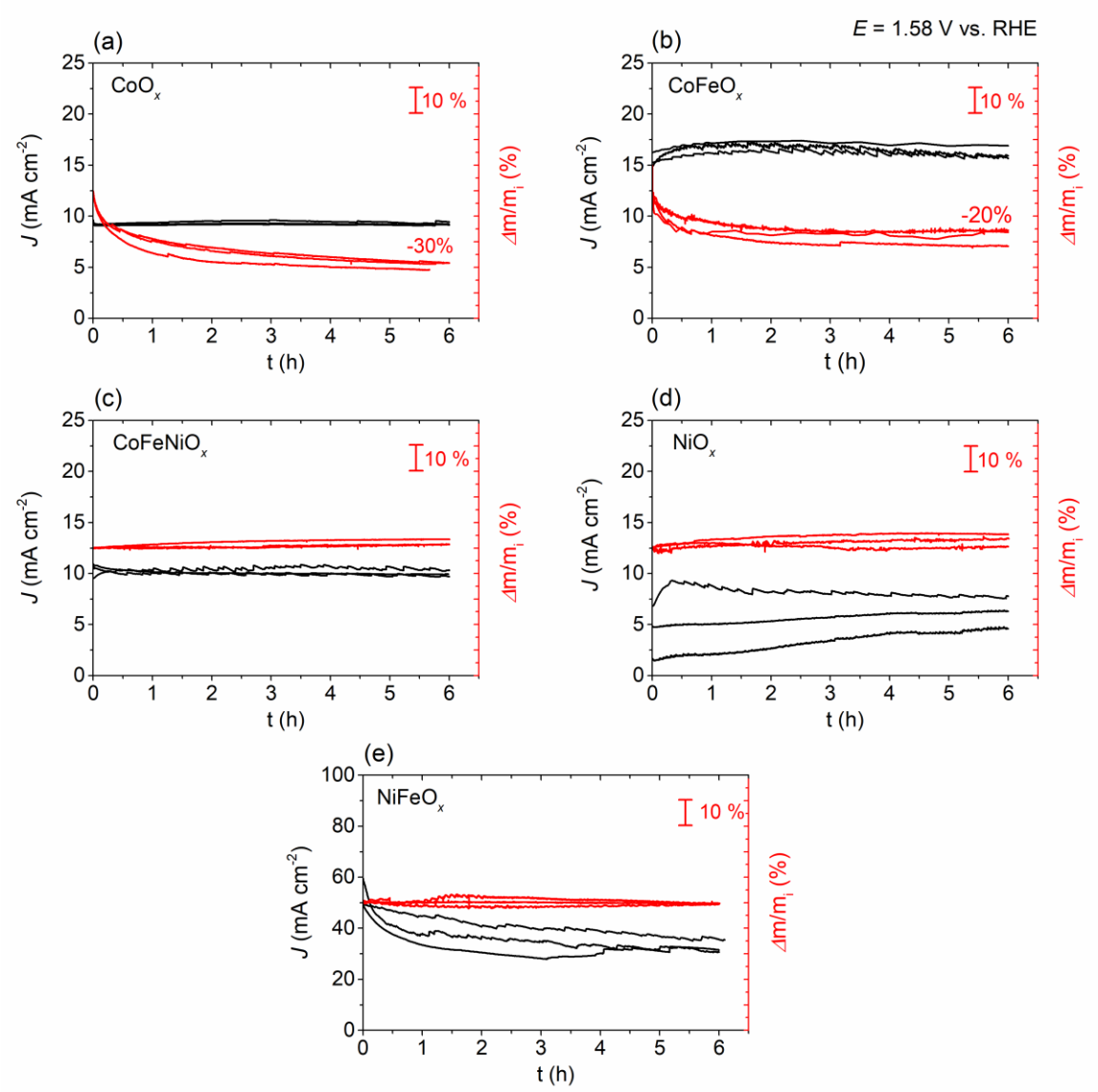

Figure 5. (a)-(e) Evolution of current density and mass of the five catalysts during electrolysis at a constant potential of 1.58 V in 1 M KOH during 6 hours. The evolution of mass was determined by eQCM. Three samples were measured for each catalyst.

According to eQCM, the mass of CoO_x and $CoFeO_x$ decreased by 20 to 30% during 6 h of potentiostatic electrolysis while those of $CoFeNiO_x$, NiO_x, and $NiFeO_x$ remained largely the same (Figure 5). ICP-OES measurements indicated again that eQCM sometimes failed to give accurate values of total mass change (Figure 6). According to ICP-OES, only $CoFeO_x$ had a significantly lower total mass (25–35%) after 6 h of potentiostatic

electrolysis (Figure 6b). For other catalysts the total mass remained similar within the errors of experiments (Figure 6a, 6c-e6). The change in total mass did not completely reflect the change in individual metal concentrations for some catalysts. For example, for CoO_x, the change of total mass was in the range of 10%, but the mass of Co ions decreased by 20–30%. The difference was due to the incorporation of Fe ions in CoO_x (Figure 6a). A similar, but less significant composition change was observed for $CoFeO_x$ and $NiFeO_x$ (Figure 6b and 6e). For $CoFeNiO_x$, Ni seemed to be enriched at the expense of Fe (Figure 6c). Like in galvanostatic electrolysis, the incorporation of Fe into NiO_x did not lead to substantial change of the total mass (Figure 6d).

We noticed some different EQCM responses when electrolysis was conducted under galvanostatic or potentiostatic conditions. The geometric current density during potentiostatic electrolysis about 2-3 times higher than that during galvanostatic electrolysis. The different electrochemical conditions might lead to different response factors of eQCM.

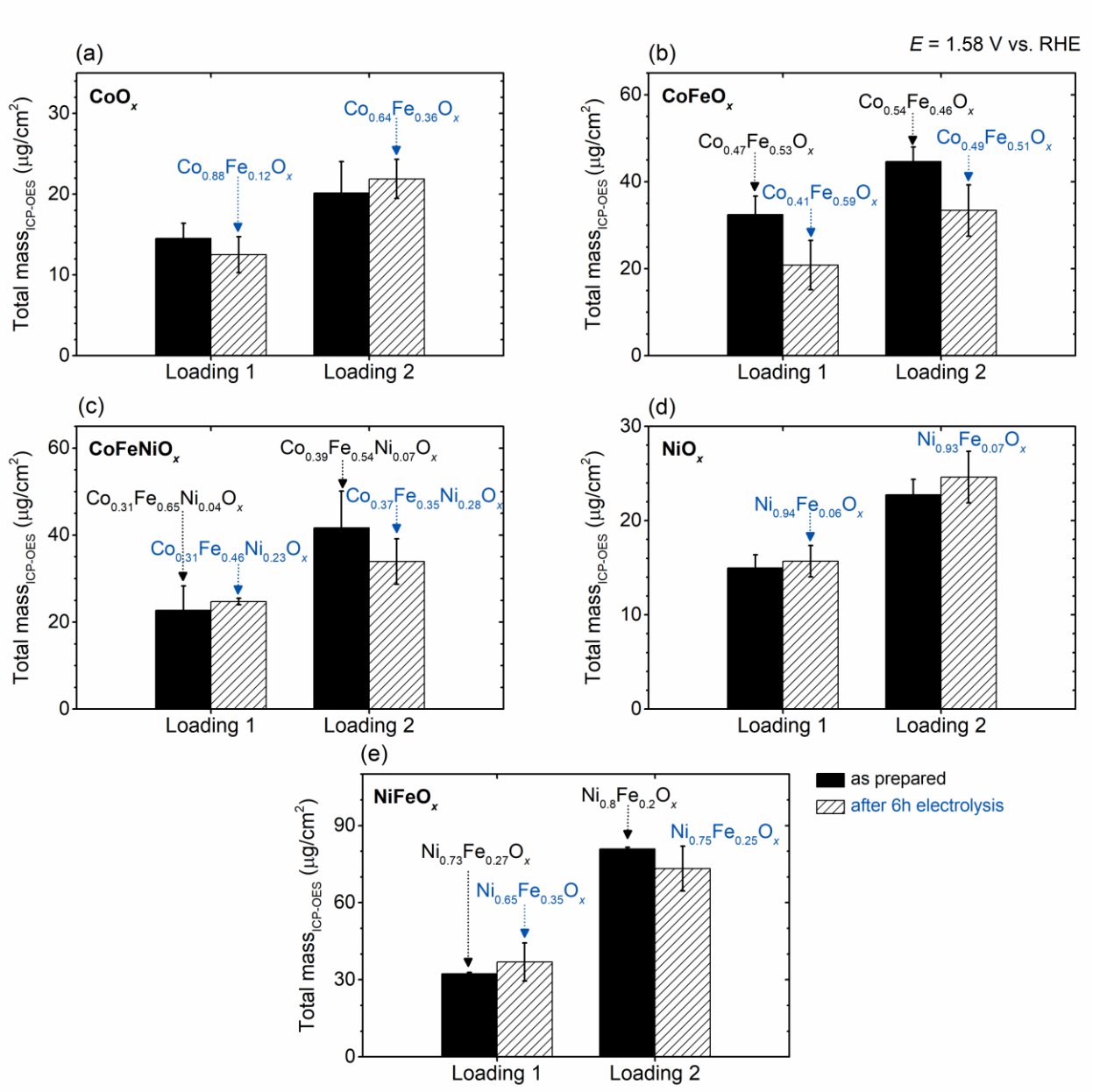

Figure 6. (a)-(f) Comparison of the ICP-OES determined mass of the catalyst before and after electrolysis at a constant potential of 1.58 V vs. RHE for 6 hours in 1 M KOH. The composition of the catalysts before and after catalysis is indicated. Two samples were measured for each loading; the error bar represents standard deviation.

Electrochemical impedance spectroscopic analysis of catalysts during galvanostatic electrolysis. Electrochemical impedance spectroscopy (EIS) analysis was conducted to probe the changes of several properties of the catalysts including capacitance, charge transfer resistance, and electrochemical surface area (ECSA).[52] The equivalent circuit

used to model the EIS data is shown in Figure 7a.[28,36,53] R_e corresponds to the electrolyte resistance and R_{ct} represents the charge transfer resistance of OER. The double layer capacitance, C_{dl}, is modelled by a constant phase element (CPE) with its components $Q_{\underline{dl}}$ and α_{dl}.[52] The equivalent circuit includes a second characteristic time constant, where R_f represents the electron transfer resistance through the catalyst film and through the electrode/catalyst interface. The capacitance of the electrode/catalyst interface is simulated by another CPE with its components $Q_{\underline{f}}$ and α_f. Figure 7b shows both Nyquist and Bode plots for CoO_x that was subjected to extended electrolysis at a constant current density of 5 mA cm^{-2} as a representative example of the fitting quality. Similar plots for the other catalysts are shown in Figures S16a–d, SI.

As shown in Figure 8, the evolution of the catalytic activity during the first 6 h was in agreement with the results in Figure 3. After 6 h, the activity, as measured by the overpotential, remained constant for the next 8 h for all catalysts. The Tafel slopes for all but one catalysts remain relatively stable during the 14 h electrolysis (Figure 8 and Table S1, SI; see Figure S17 for corresponding LSV curves). The exception was NiO_x, whose Tafel slope decreased from about 58 mV/dec to 40 mV/dec. This decrease was due to the incorporation of Fe ions.

The ECSAs of CoO_x, NiO_x, and $NiFeO_x$ had insignificant changes during 14 h (Figure 8 and Table S1, SI). Those of $CoFeO_x$ and $CoFeNiO_x$, however, increased by about 40% and 10%, respectively (Figure 8 and Table S1, SI). Again, the changes occurred within the first 6 h. The charge transfer resistance, which reflects the OER kinetics, had more catalyst-specific changes. For all catalysts but $NiFeO_x$, the resistance decreased within the first 3 h to a steady-state value. For $NiFeO_x$, the charge transfer resistance remained nearly constant except a small increase in the first hour. The charge transfer resistance decreased by 50% for NiO_x due to Fe incorporation. Unexpectedly, the charge transfer resistance decreased by 40% for $CoFeO_x$ and by 20% for the other two Co-containing catalysts.

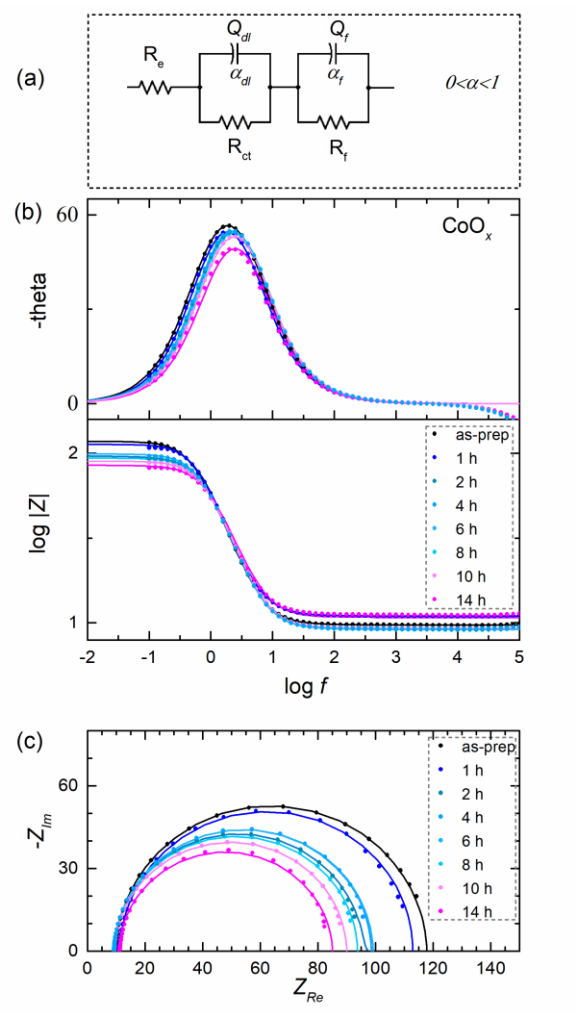

Figure 7. (a) Equivalent circuit for the fitting of impedance data; (b) and (c) The Bode and Nyquist plots for CoO_x.

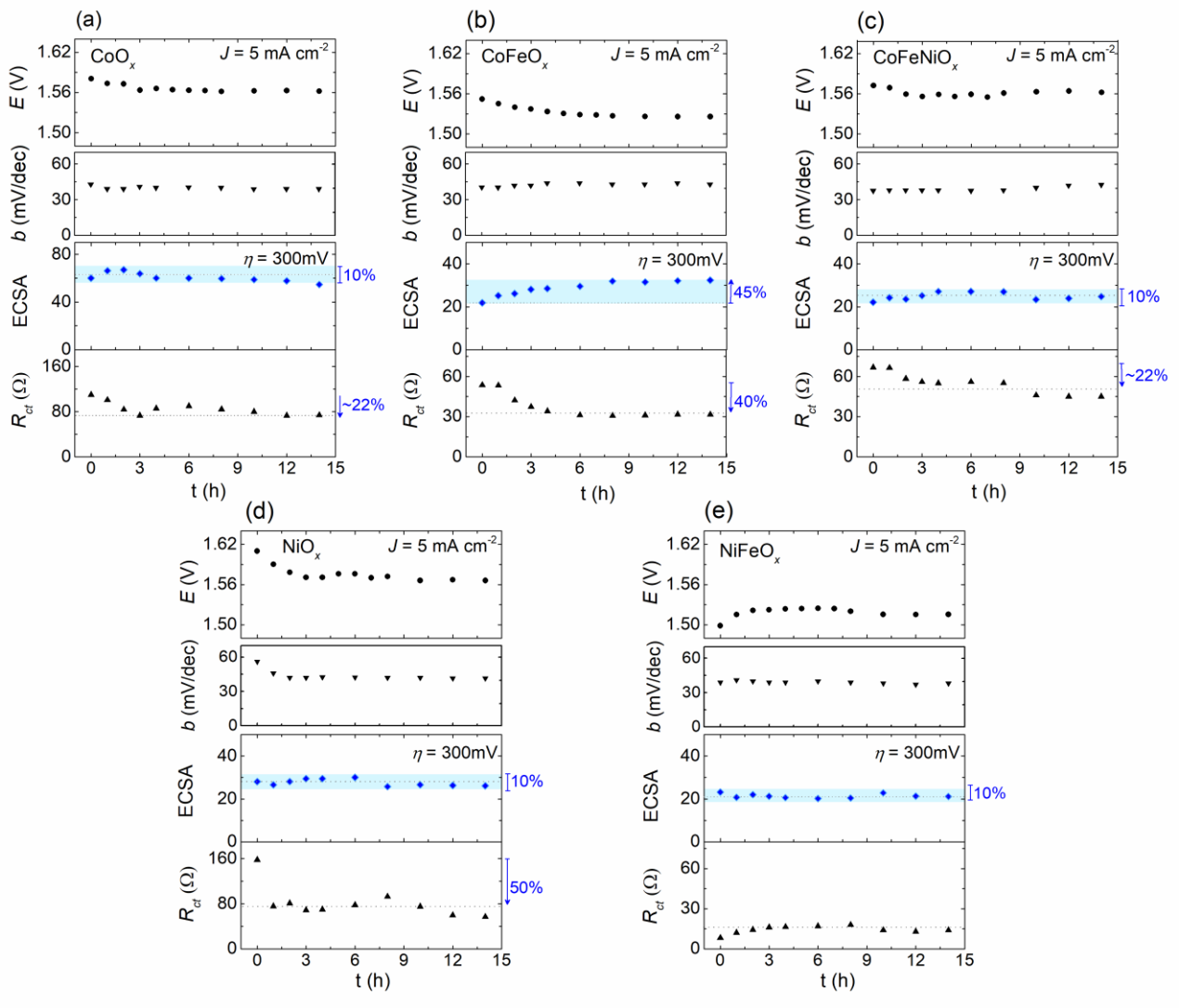

Figure 8. (a-e) Evolution of potentials (E, V), Tafel slopes (b, mV/dec), ECSA (cm^2), and charge transfer resistance (R_{ct}, Ω), for the five catalysts during 14 h of electrolysis at 5 mA/cm^2. All potentials are referenced to RHE.

DISCUSSION

Limitation of eQCM. While eQCM can be used for *in-situ* monitoring of OER catalysts, the comparison of results from eQCM and ICP-OES indicates a severe limitation of eQCM in the study of the stability of OER catalysts. Non-flat surface, uneven deposition, change of viscoelastic properties, adsorption of ions and molecules, and bubble formation are all possible factors that lead to non-ideal eQCM response.[25,38] For the deposition of a same metal oxide, eQCM gives qualitatively correct information on the mass of the oxide due to a linear scaling of the eQCM

mass with the actual mass (represented by ICP-OES data). However, the scaling factors are different for different oxides (Figure 1). For the evolution of the mass of catalysts during OER, there is no correlation of eQCM results with actual mass change. This conclusion is illustrated in Figure 9, where values of +1, 0, -1 are assigned to mass increase, stable, and decrease, respectively. Even qualitatively, the results from eQCM are drastically different from those measured by ICP-OES. Our results are in line with an earlier study indicating the limitation of eQCM.[27] Thus, we caution the general use of eQCM in the study of stability of OER catalysts.

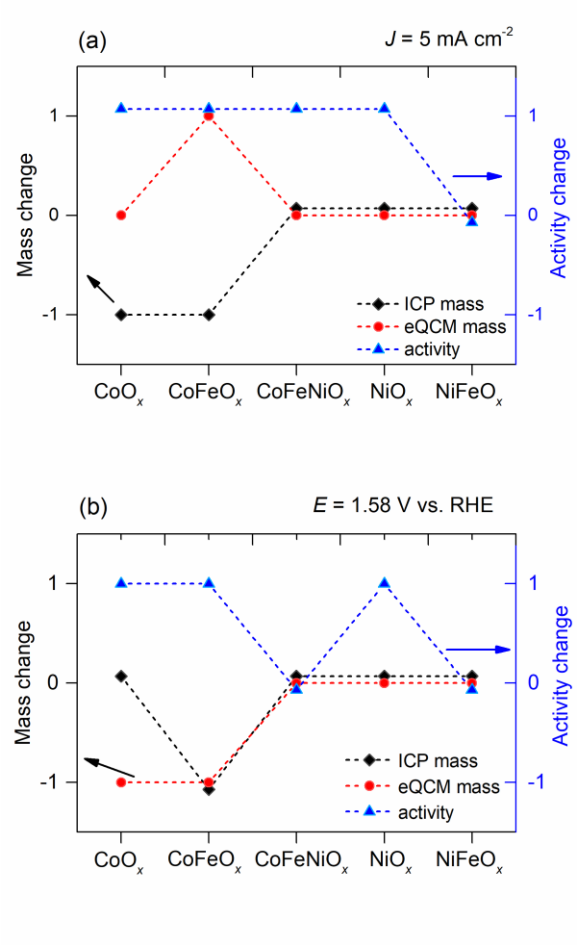

Figure 9. Correlation of the changes in mass (determined by eQCM and ICP) as well as catalytic activity for the five electrocatalysts after 6 h electrolysis at (a) constant current density J = 5 mA cm^{-2}, and (b) constant potential E = 1.58 V vs. RHE. Values of +1, 0, -1 are assigned to substantial increase, stable, and substantial decrease, respectively.

Does activity indicate stability? The activity in galvanostatic or potentiostatic electrolysis is commonly used in the literature as a measure of the stability of OER catalysts. Figure 9 compares qualitatively the evolutions of activity and mass changes of the five catalysts investigated here. No correlation exists between the activity and mass changes, indicating activity as a poor metric for stability. Our study provides several examples illuminating the

various origins of this non-correlation. For CoO_x in normal and Fe-containing KOH, a small amount of Fe is incorporated during electrolysis, which significantly increases the activity. At the same time, a substantial dissolution of CoO_x occurs so the total mass actually decreases. For CoO_x in Fe-free and Co-containing KOH, the activity is stable, but more CoO_x is deposited during electrolysis. In both cases, activity and stability are not correlated because the intrinsic activity, active site, or both are changed in a non-linear manner with respect to mass change.

Mass and compositional changes during OER. Figure 10 summarizes the mass changes for the five catalysts after 6 h of electrolysis. After galvanostatic electrolysis, the masses of CoO_x and $CoFeO_x$ decreased by about 20%, indicating substantial instability (Figure 10a). The masses of $CoFeNiO_x$, NiO_x, and $NiFeO_x$ remained largely constant. After potentiostatic electrolysis, only $CoFeO_x$ lost about 20% of its mass, while the other catalysts maintained their initial masses (Figure 10b). Thus, the stability profile of a same catalyst might vary under different electrochemical conditions. This difference might be due to a potential-dependent decomposition of a catalyst. In any case, $CoFeO_x$ appeared to be the least stable with respect to mass change.

Our ICP-OES data reveal that the composition of a catalyst might change while its total mass remains nearly constant. In fact, all catalysts underwent noticeable compositional changes during both galvanostatic and potentiostatic electrolysis (Figures 4 and 6). The incorporation of residual Fe ions from the electrolyte solution was a common origin of this change. The Fe incorporation was in many cases balanced by dissolution of another metal ions so that the total mass remained constant. For $CoFeNiO_x$, the amount of Fe actually decreased probably due to dissolution of a separate, unstable Fe-rich oxide phase.[23,54] The compositional analysis show that all five oxide catalysts are prone to dynamic exchanges of metal ions with the electrolyte solutions.

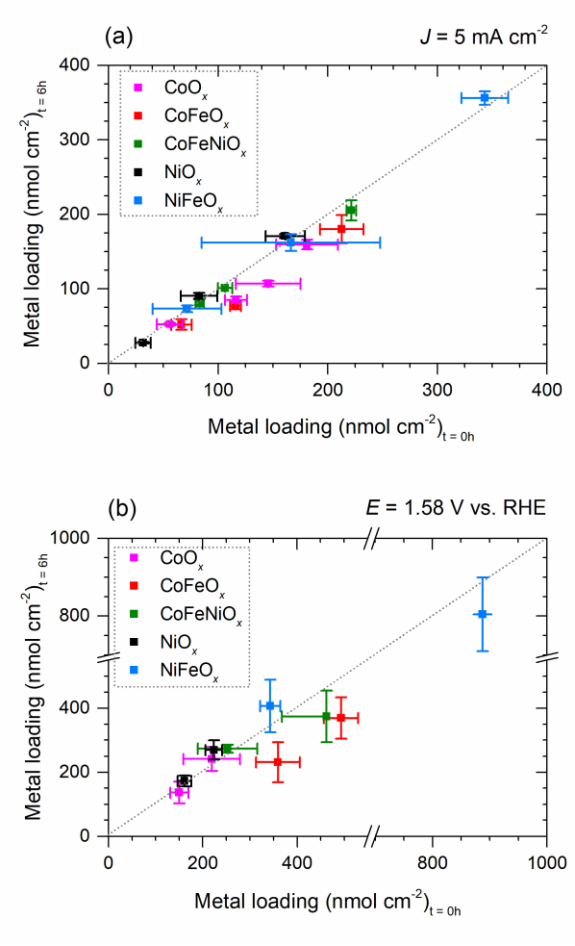

Figure 10. Mass loadings of the electrocatalysts as detected by ICP-OES for as prepared and after 6h electrolysis samples; (a) galvanostatic electrolysis at 5 mA cm^{-2}, and (b) potentiostatic electrolysis at 1.58 V vs. RHE.

Insights from EIS. The EIS analysis reveals that after 3-6 h of galvanostatic electrolysis, the activity, Tafel slope, ECSA, and charge transfer resistance reach stead-state values for all catalysts. This result suggests the dynamic exchange of metal ions approaches an equilibrium after 6 h. The EIS data give insights into the changes of the catalysts during electrolysis. For CoO_x, partial dissolution of CoO_x and incorporation of Fe occurred at the same time. The ECSA remained similar, suggesting that the newly transformed catalyst was slightly more porous (as it weighted 20% less). The drop in charge transfer resistance was due to Fe incorporation, since $CoFeO_x$ was known to be more active than CoO_x.[24] For $CoFeO_x$, the same process as in CoO_x occurred, but the ECSA was significantly increased suggesting a much more porous catalyst. The significant decrease in charge transfer resistance suggests that new active sites were created due to having a more porous structure. For $CoFeNiO_x$, a nearly synchronous change in ECSA and charge transfer resistance was observed, suggesting a morphological/compositional change that led to a more porous catalyst. For NiO_x, a trace amount of Fe was incorporated without changing the ECSA

but significantly decreased charge transfer resistance due to the formation of more active reaction sites as previously reported.[31,55] For $NiFeO_x$, only minor changes were observed in ECSA and charge transfer resistance, suggesting that the compositional change due to dynamic exchanges of metal ions with the electrolyte solution had little consequence in the number and activity of active sites.

Mechanism of dissolution and ion exchange. The compositional changes of catalysts during electrolysis is a result of dissolution of certain metal oxides (e.g., CoO_x) and incorporation of Fe ions. Thermodynamically these processes should be governed by the Pourbaix diagram.[56] Under OER conditions the classic Pourbaix diagram suggests Co ions should exist in a solid form of $Co(OH)_3$, but a more recent study suggests that Co might exist as Co_3O_4, CoOOH, and at highly oxidative potentials soluble species $CoOH^{2+}$ becomes stable.[57] The dissolution of CoO_x in Co-containing catalysts in the initial period of electrolysis (6 h) might reflect the process to reach equilibrium of solid and soluble Co species. As the catalysts are amorphous and inhomogeneous in composition and phase, the amount of dissolution and the final composition will vary among different samples, as observed in our study. The Pourbaix diagram of Fe suggests that under OER conditions Fe_2O_3 is most stable, but the formation of soluble FeO_4^{2-} becomes possible at high oxidative potentials.[58] The incorporation of Fe into the lattice of metal oxides from electrolyte solutions under OER is consistent with the thermodynamic tendency of the Fe-H_2O system. At a low doping level of Fe, the Fe ions likely replace the existing metal ions, which are under a dynamic equilibrium of dissolution/deposition (e.g., Co). The overall morphology and structures are maintained, as observed by SEM. According to a recent Pourbaix diagram, under OER conditions Ni should exist as NiOOH, NiO_2, or both.[59] These nickel oxides are stable solids. Consistent with this Pourbaix diagram, no significant dissolution of NiO_x in Ni-containing catalysts was observed in our study. Fe ions are probably incorporated in the defect sites, which should be abundant in amorphous films.

Kinetic processes might also lead to dissolution and ion exchange. For example, OER can create oxygen vacancies at either the surface or the bulk. M-O units near the vacancies might be less stable and subject to dissolution. The vacancies are also nucleation sites for the incorporation of new M-O units. An example of such process in a perovskite OER precatalyst was recently reported.[17] Thus, even if an oxide phase is thermodynamically stable according to Pourbaix diagram. We suspect that Fe-incorporation in Ni-based catalysts occurs via this pathway.

CONCLUSIONS

The stability profile of five representative metal oxides during OER in alkaline medium is studied by a combination of eQCM, ICP-OES, and EIS under both galvanostatic and potentiostatic conditions. eQCM was found not suitable for measuring the mass of the catalysts during OER due to non-ideal response. According to ICP-OES, CoO_x and $CoFeO_x$ lose mass while $CoFeNiO_x$, NiO_x, $NiFeO_x$ maintain their mass during OER. The mass change can be different for the same catalyst when subjected to different electrochemical conditions, suggesting that decomposition can be potential-dependent. There is no correlation between stability of activity and stability of catalyst mass, confirming that activity is not a valid metric for stability. ICP-OES data also reveal that all five oxides undergo compositional changes during OER due to a dynamic exchange of metal ions with the electrolyte solutions. Fe incorporation and partial dissolution of CoO_x are two predominant examples of such exchange. Electrochemical data collected over an extended period of electrolysis (14 h) indicate that this dynamic exchange reaches a steady-state after 6 h. Analysis of ECSA and charge transfer resistance obtained from EIS reveals different microscopic changes for different catalysts. For Fe-free CoO_x and NiO_x, incorporation of Fe ions significantly increased the activity without altering the ECSA. For $CoFeO_x$ and $CoFeNiO_x$, the catalysts undergo an initial activation, which leads to a higher ECSA (20-40%) without changing the active sites. For $NiFeO_x$, both active sites and ECSA are maintained.

Our study reveals a complex, catalyst-dependent stability profile for metal oxides in OER. A dynamic exchange of metal ions between the catalysts and the electrolyte solutions causes compositional instability in the initial period of catalysis, however, a steady-state equilibrium is reached after 6 h. The catalysts are then considered as stable. Adding a trace amount of appropriate metal ions in the electrolyte solutions might increase the stability in the initial period.

ACKNOWLEDGMENTS

This project has received funding from the European Research Council (no. 681292) under the European Union's Horizon 2020 research and innovation program. We thank Dr. Natalia Gasilova (EPFL) for the ICP measurements and Dr. Pascal Alexander Schouwink (EPFL) for the XRD analysis.

REFERENCES

1 N. S. Lewis and D. G. Nocera, *Proc. Natl. Acad. Sci.*, 2006, **103**, 15729–15735.
2 S. Chu and A. Majumdar, *Nature*, 2012, **488**, 294–303.
3 N. S. Lewis, *Science*, 2016, **351**, aad1920.
4 B. M. Hunter, H. B. Gray and A. M. Müller, *Chem. Rev.*, 2016, **116**, 14120–14136.
5 F. Song, L. Bai, A. Moysiadou, S. Lee, C. Hu, L. Liardet and X. Hu, *J. Am. Chem. Soc.*, 2018, **140**, 7748–7759.
6 H. Dau, C. Limberg, T. Reier, M. Risch, S. Roggan and P. Strasser, *ChemCatChem*, 2010, **2**, 724–761.
7 F. Song, M. M. Busch, B. Lassalle-Kaiser, C.-S. Hsu, E. Petkucheva, M. Bensimon, H. M. Chen, C. Corminboeuf and X. Hu, *ACS Cent. Sci.*, 2019, *5*, 558-568.
8 L. Trotochaud, J. K. Ranney, K. N. Williams and S. W. Boettcher, *J. Am. Chem. Soc.*, 2012, **134**, 17253–17261.
9 C. Roy, B. Sebok, S. B. Scott, E. M. Fiordaliso, J. E. Sørensen, A. Bodin, D. B. Trimarco, C. D. Damsgaard, P. C. K. Vesborg, O. Hansen, I. E. L. Stephens, J. Kibsgaard and I. Chorkendorff, *Nat. Catal.*, 2018, **1**, 820.
10 N.-T. Suen, S.-F. Hung, Q. Quan, N. Zhang, Y.-J. Xu and H. Ming Chen, *Chem. Soc. Rev.*, 2017, **46**, 337–365.
11 F. Dionigi and P. Strasser, *Adv. Energy Mater.*, 2016, **6**, 1600621.
12 F. Lyu, Q. Wang, S. M. Choi and Y. Yin, *Small*, 2019, **15**, 1804201.
13 S. Cherevko, A. R. Zeradjanin, A. A. Topalov, N. Kulyk, I. Katsounaros and K. J. J. Mayrhofer, *ChemCatChem*, 2014, **6**, 2219–2223.
14 M. B. Stevens, L. J. Enman, A. S. Batchellor, M. R. Cosby, A. E. Vise, C. D. M. Trang and S. W. Boettcher, *Chem. Mater.*, 2017, **29**, 120–140.
15 S. Geiger, O. Kasian, A. M. Mingers, S. S. Nicley, K. Haenen, K. J. J. Mayrhofer and S. Cherevko, *ChemSusChem*, 2017, **10**, 4140–4143.
16 Y.-T. Kim, P. P. Lopes, S.-A. Park, A.-Y. Lee, J. Lim, H. Lee, S. Back, Y. Jung, N. Danilovic, V. Stamenkovic, J. Erlebacher, J. Snyder and N. M. Markovic, *Nat. Commun.*, 2017, **8**, 1–8.
17 E. Fabbri, M. Nachtegaal, T. Binninger, X. Cheng, B.-J. Kim, J. Durst, F. Bozza, T. Graule, R. Schäublin, L. Wiles, M. Pertoso, N. Danilovic, K. E. Ayers and T. J. Schmidt, *Nat. Mater.*, 2017, **16**, 925–931.
18 K. J. May, C. E. Carlton, K. A. Stoerzinger, M. Risch, J. Suntivich, Y.-L. Lee, A. Grimaud and Y. Shao-Horn, *J. Phys. Chem. Lett.*, 2012, **3**, 3264–3270.
19 C. C. L. McCrory, S. Jung, J. C. Peters and T. F. Jaramillo, *J. Am. Chem. Soc.*, 2013, **135**, 16977–16987.
20 S. Cherevko, S. Geiger, O. Kasian, N. Kulyk, J.-P. Grote, A. Savan, B. R. Shrestha, S. Merzlikin, B. Breitbach, A. Ludwig and K. J. J. Mayrhofer, *Catal. Today*, 2016, **262**, 170–180.
21 I. Spanos, A. A. Auer, S. Neugebauer, X. Deng, H. Tüysüz and R. Schlögl, *ACS Catal.*, 2017, **7**, 3768–3778.
22 A. R. Hillman, *J. Solid State Electrochem.*, 2011, **15**, 1647–1660.
23 S. Zou, M. S. Burke, M. G. Kast, J. Fan, N. Danilovic and S. W. Boettcher, *Chem. Mater.*, 2015, **27**, 8011–8020.
24 M. S. Burke, S. Zou, L. J. Enman, J. E. Kellon, C. A. Gabor, E. Pledger and S. W. Boettcher, *J. Phys. Chem. Lett.*, 2015, **6**, 3737–3742.
25 D. A. Buttry and M. D. Ward, *Chem. Rev.*, 1992, **92**, 1355–1379.
26 M.-S. Kim, T.-S. Hwang and K.-B. Kim, *J. Electrochem. Soc.*, 1997, **144**, 1537–1543.

27 R. Frydendal, E. A. Paoli, B. P. Knudsen, B. Wickman, P. Malacrida, I. E. L. Stephens and I. Chorkendorff, *ChemElectroChem*, 2014, **1**, 2075–2081.
28 C. G. Morales-Guio, L. Liardet and X. Hu, *J. Am. Chem. Soc.*, 2016, **138**, 8946–8957.
29 H. Vrubel, T. Hasegawa, E. de Oliveira and F. S. Nunes, *Inorg. Chem. Commun.*, 2006, **9**, 208–211.
30 R. Weinland and H. Holtmeier, *Z. Für Anorg. Allg. Chem.*, 1928, **173**, 49–62.
31 L. Trotochaud, S. L. Young, J. K. Ranney and S. W. Boettcher, *J. Am. Chem. Soc.*, 2014, **136**, 6744–6753.
32 G. H. A. Therese and P. V. Kamath, *Chem. Mater.*, 2000, **12**, 1195–1204.
33 J. R. S. Brownson and C. Lévy- Clément, *Phys. Status Solidi B*, 2008, **245**, 1785–1791.
34 M. S. Burke, M. G. Kast, L. Trotochaud, A. M. Smith and S. W. Boettcher, *J. Am. Chem. Soc.*, 2015, **137**, 3638–3648.
35 S. Jung, C. C. L. McCrory, I. M. Ferrer, J. C. Peters and T. F. Jaramillo, *J. Mater. Chem. A*, 2016, **4**, 3068–3076.
36 P. Chakthranont, J. Kibsgaard, A. Gallo, J. Park, M. Mitani, D. Sokaras, T. Kroll, R. Sinclair, M. B. Mogensen and T. F. Jaramillo, *ACS Catal.*, 2017, **7**, 5399–5409.
37 W. T. Hong, M. Risch, K. A. Stoerzinger, A. Grimaud, J. Suntivich and Y. Shao-Horn, *Energy Environ. Sci.*, 2015, **8**, 1404–1427.
38 I. Efimov, A. R. Hillman and J. Walter Schultze, *Electrochimica Acta*, 2006, **51**, 2572–2577.
39 M. D. Ward and D. A. Buttry, *Science*, 1990, **249**, 1000–1007.
40 G. T. Cheek and W. E. O'Grady, *J. Electroanal. Chem.*, 1997, **421**, 173–177.
41 J. Yang, H. Liu, W. N. Martens and R. L. Frost, *J. Phys. Chem. C*, 2010, **114**, 111–119.
42 M. C. Biesinger, B. P. Payne, A. P. Grosvenor, L. W. M. Lau, A. R. Gerson and R. St. C. Smart, *Appl. Surf. Sci.*, 2011, **257**, 2717–2730.
43 J. A. Koza, Z. He, A. S. Miller and J. A. Switzer, *Chem. Mater.*, 2012, **24**, 3567–3573.
44 W. P. Wang, H. Yang, T. Xian and J. L. Jiang, *Mater. Trans.*, 2012, **53**, 1586–1589.
45 L. Liardet, J. E. Katz, J. Luo, M. Grätzel and X. Hu, *J. Mater. Chem. A*, 2019, **7**, 6012–6020.
46 H. Ali-Löytty, M. W. Louie, M. R. Singh, L. Li, H. G. Sanchez Casalongue, H. Ogasawara, E. J. Crumlin, Z. Liu, A. T. Bell, A. Nilsson and D. Friebel, *J. Phys. Chem. C*, 2016, **120**, 2247–2253.
47 X. Xu, F. Song and X. Hu, *Nat. Commun.*, 2016, **7**, 12324.
48 A. P. Grosvenor, M. C. Biesinger, R. St. C. Smart and N. S. McIntyre, *Surf. Sci.*, 2006, **600**, 1771–1779.
49 D. A. Corrigan, *J. Electrochem. Soc.*, 1987, **134**, 377.
50 D. A. Corrigan and R. M. Bendert, *J. Electrochem. Soc.*, 1989, **136**, 723–728.
51 M. Wehrens-Dijksma and P. H. L. Notten, *Electrochimica Acta*, 2006, **51**, 3609–3621.
52 G. J. Brug, A. L. G. van den Eeden, M. Sluyters-Rehbach and J. H. Sluyters, *J. Electroanal. Chem. Interfacial Electrochem.*, 1984, **176**, 275–295.
53 R. L. Doyle and M. E. G. Lyons, *Phys. Chem. Chem. Phys.*, 2013, **15**, 5224–5237.
54 M. S. Burke, L. J. Enman, A. S. Batchellor, S. Zou and S. W. Boettcher, *Chem. Mater.*, 2015, **27**, 7549–7558.
55 S. Klaus, Y. Cai, M. W. Louie, L. Trotochaud and A. T. Bell, *J. Phys. Chem. C*, 2015, **119**, 7243–7254.
56 M. J. N. Pourbaix and N. de Zoubov, *Atlas d'equilibres electrochimiques*, Gauthier-Villars, Paris, 1963.
57 J. Chivot, L. Mendoza, C. Mansour, T. Pauporté and M. Cassir, *Corros. Sci.*, 2008, **50**, 62–69.
58 B. Beverskog and I. Puigdomenech, *Corros. Sci.*, 1996, **38**, 2121–2135.
59 L.-F. Huang, M. J. Hutchison, R. J. Santucci, J. R. Scully and J. M. Rondinelli, *J. Phys. Chem. C*, 2017, **121**, 9782–9789.